Materials Science & Engineering A 893 (2024) 146107

Contents lists available at ScienceDirect

Materials Science & Engineering A

journal homepage: www.elsevier.com/locate/msea

Supreme tensile properties in precipitation-hardened 316L stainless steel fabricated through powder cold-consolidation and annealing

Do Won Lee [a], Peyman Asghari-Rad [a,**], Yoon-Uk Heo [b], Sujung Son [a], Hyojin Park [a], Ji-Su Lee [a], Jae-il Jang [c], Byeong-Joo Lee [a], Hyoung Seop Kim [a,b,d,e,f,*]

[a] Department of Materials Science and Engineering, Pohang University of Science and Technology (POSTECH), Pohang, 37673, South Korea
[b] Graduate Institute of Ferrous Technology, Pohang University of Science and Technology (POSTECH), Pohang, 37673, South Korea
[c] Division of Materials Science and Engineering, Hanyang University, Seoul, 04763, South Korea
[d] Center for Heterogenic Metal Additive Manufacturing, Pohang University of Science and Technology (POSTECH), Pohang, 37673, South Korea
[e] Advanced Institute for Materials Research (WPI-AIMR), Tohoku University, Sendai, 980-8577, Japan
[f] Center Institute for Convergence Research and Education in Advanced Technology, Yonsei University, Seoul, 03722, South Korea

ARTICLE INFO

Keywords:
Powder metallurgy
High-pressure torsion
Cold-consolidation
Sigma phase precipitation
Grain refinement

ABSTRACT

One of the key goals of processing 316L stainless steel by powder metallurgy (PM) techniques is to achieve industrial-viable tensile properties without structural defects like poor densification, undesired phase transitions, and oxidation during high-temperature sintering. To address this, this study adopts high-pressure torsion to fabricate a fully dense structure at ambient temperature through cold consolidation. The samples fabricated by the present PM-based technique exhibits considerably enhanced tensile properties compared to counterparts processed by conventional PM techniques, with a remarkable yield strength of 1 GPa and total elongation of 46%. Additionally, the segregation of certain elements during subsequent annealing results in a unique microstructure with nano-scale sigma precipitates which induces dislocation pile-up, leading to improved yield strength and retarded dislocation motion. The results indicate that the present PM-based route is an applicable technique to achieve the strength-ductility synergy in 316L stainless steel.

1. Introduction

316L stainless steel is one of the most widely used alloys in aerospace, marine, and automotive industries, which has excellent mechanical properties [1], and high corrosion and wear resistance [2]. As an innovative advance in processing this versatile alloy, it has been fabricated through the casting and powder metallurgy (PM) technique for various applications [3]. Alloys processed by conventional PM methods, including powder injection molding (PIM), metal injection molding (MIM) [4], and spark plasma sintering (SPS) [5] have been reported abundantly in recent years. These PM-based techniques are mostly proceeded by compacting the blended powders followed by sintering them at high temperatures. However, the alloys fabricated by the PM techniques are mostly deficient in tensile ductility compared to the casting counterpart and not preferentially favorable for structural applications [6]. The lack of tensile elongation in the PM-processed alloys is attributed to their pores, contamination, undesired phase transition, and oxidation during sintering at high temperatures [7].

To achieve the sought tensile properties using the PM processes, the pores should be minimized, and the processing temperature needs to be reduced to prevent unwanted phase transformations and oxidation. Utilizing severe plastic deformation (SPD) such as high-pressure torsion (HPT) on powders can lead to a dense structure at room temperature. Powder HPT processing can impose an intensive strain, resulting in nanocrystalline microstructures. However, the HPT-processed specimens commonly present limited ductility due to the HPT-induced high (usually upper limit) dislocation density. Therefore, subsequent annealing is useful for fine-tuning the dislocation density to recover the ductility. This post-HPT annealing should be conducted at a lower temperature and short annealing time to maintain the nano/ultrafine grains by avoiding grain growth, which is notably lower than the conventional sintering temperature. The feasibility of this novel cold

* Corresponding author. Department of Materials Science and Engineering, Pohang University of Science and Technology (POSTECH), Pohang, 37673, South Korea.
** Corresponding author.
E-mail addresses: peyman.asghari.rad@gmail.com (P. Asghari-Rad), hskim@postech.ac.kr (H.S. Kim).

https://doi.org/10.1016/j.msea.2024.146107
Received 3 June 2023; Received in revised form 26 December 2023; Accepted 7 January 2024
Available online 8 January 2024
0921-5093/© 2024 Elsevier B.V. All rights reserved.

consolidation technique was verified by the fabrication of high/medium entropy alloys [8,9], composites [10,11], and layered structures [12,13] with superior mechanical properties.

In the present study, we attempt to fabricate 316L stainless steel with a single face-centered cubic (FCC) phase using the novel PM-based fabrication route to achieve a nanocrystalline microstructure, while the post-HPT annealing is generally feasible to generate a secondary phase such as sigma (σ) phase. It was reported that coarse precipitation of σ phase in duplex stainless steels deteriorates the mechanical properties due to its brittle and incoherent features [14–16]. Therefore, it is noted how the σ phase contributes to the tensile properties and the microstructure in this technique.

2. Experimental procedure

2.1. Sample preparation

As-received gas-atomized 316L stainless steel powders with the chemical composition shown in Table 1 were used. The powders are nearly spherical with an average diameter of ~92.62 μm measured with the powder size analyzer (Malvern, Master size 2000) as shown in Fig. 1.

The powders were put into cylinder-shaped rods and were pre-compacted under a pressure of 20 MPa operated by a press machine to produce the disk-shaped samples with 10 mm in diameter and 2 mm in thickness. All of the samples were subject to the HPT process at a pressure of 5 GPa and 4 turns with speeds of 1 revolution per minute. An entire schematic of powder cold consolidation using HPT is illustrated in Fig. 2a. Then, post-HPT annealing was subsequently operated on the HPT-processed samples at 700 °C for 15 min (A700-15) and 1 h (A700-60) and at 800 °C for 15 min (A800-15) and 1 h (A800-60) under Ar atmosphere. The annealed samples were manufactured into dog-bone-shaped specimens with 1.5 mm in gauge length and 0.7 mm in thickness at 2.5 mm far from the center (Fig. 2b).

2.2. Microstructure characterization

The microstructural investigation was analyzed by field emission scanning electron microscope (FE-SEM, JEOL-7100F, JEOL, Japan) equipped with backscattered electron (BSE), electron dispersive X-ray spectroscopy (EDS), and electron backscatter diffraction (EBSD) detectors. The phase evolution was characterized by synchrotron X-ray diffraction (XRD, 8D XRS, Pohang Accelerator Laboratory, the Republic of Korea, filtered with Si(111) monochromator, $\lambda = 1.5404$ Å). The convolutional multiple whole profile (CMWP) method was conducted on the result of X-ray line profile analysis (XLPA) to evaluate the dislocation density in the as-HPT and A700-60 samples. Also, a time-temperature-transformation (TTT) curve is calculated by ThermoCalC software based on TCFE11 and MOBFE6 databases for clarifying the precipitation of sigma phase. Transmission electron microscopy (TEM, JEM-2100F, JEOL, Japan) was operated to analyze the effect of precipitates on the microstructure with scanning transmission electron microscopy bright field (BF) images and selected area diffraction (SAED) patterns of the precipitates. The TEM sample was thinned using mechanical polishing until a thickness below 90 μm, followed by jet-polishing in a solution of 90 % CH_3COOH and 10 % $HClO_4$ on a condition of 20 V and 25 °C. ImageJ software was used to calculate the size and area fraction of the precipitates.

2.3. Mechanical testing

Vickers hardness test (Future-tech, FM-700, Japan) was measured at spacings of 0.1 mm from the center of the disk under 100 gf for 15 s.

Table 1
Chemical composition of the 316L stainless steel powders.

wt%	Fe	Ni	Cr	Mo	C	Mn	Si	P	S
316L stainless steel	Bal.	11.25	16.92	2.25	0.013	0.75	0.68	0.01	0.006

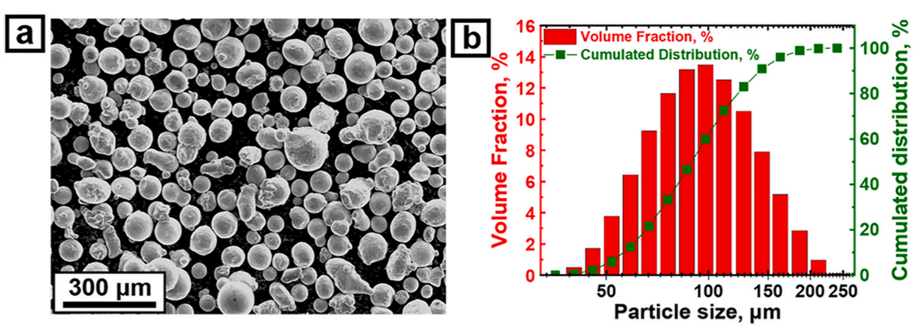

Fig. 1. (a) SEM - SE image of the gas-atomized 316L stainless steel powders, and (b) Particle size distribution of these powders.

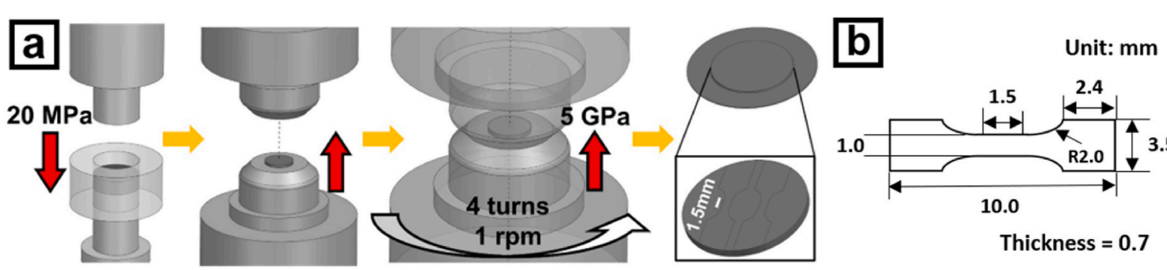

Fig. 2. (a) A schematic of powder cold consolidation using HPT, and (b) the dog-bone-shaped tensile specimen geometry fabricated by the disk samples.

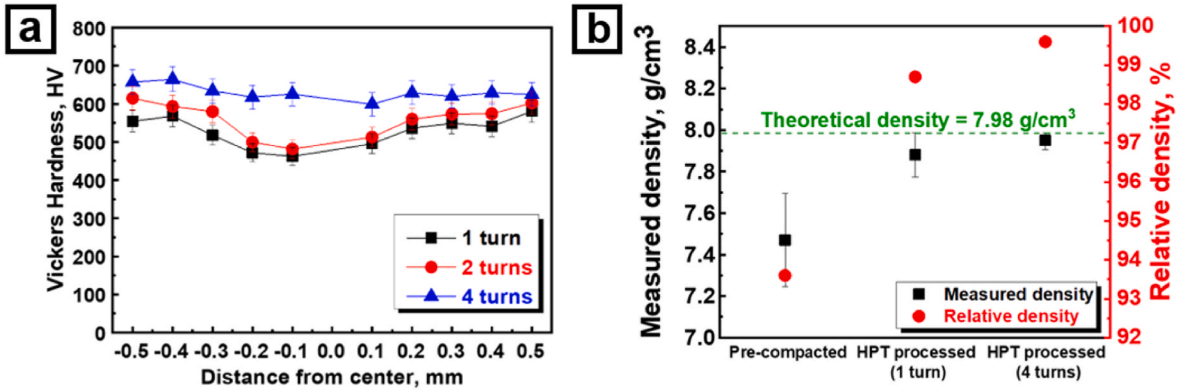

Fig. 3. (a) Microhardness distribution at each turn (1, 2, and 4 turns) of HPT across the diameters of the disk samples, and (b) density evolution at each stage (Pre-compacted, 1 turn, and 4 turns of HPT processed) of the powder HPT cold-consolidation.

Densification measurement was evaluated using the Archimedes method (METTLER TOLEDO, Balance XPR205DRV, Switzerland). The dog-bone-shaped specimens were applied on tensile tests at a strain rate of 10^{-3} s^{-1} (Instron 1361, Instron Co., Germany) with digital image correlation (DIC, ARAMIS 5 M, Germany) technique for precise strain measurement.

3. Results

3.1. Densification optimization

Fig. 3a indicates the microhardness profile at various turns (1, 2, and 4) of HPT from the center to the periphery of the disks. In the HPT-processed sample with 1 and 2 turns, the microhardness is inclined to be a non-uniform distribution which is higher prominently in the periphery region than in the center region of the disk. The higher strains exposed in the periphery region induce the non-uniform distribution of the microhardness due to the rotational nature of HPT, causing a gradient of deformation across the sample. The higher strains in the periphery result in a greater accumulation of dislocations, increased grain refinement, and subsequently higher microhardness in that region compared to the center [17]. However, the microhardness of both the center and periphery regions in the HPT-processed sample with 4 turns increases distinctly, and these values become uniformly distributed across the entire region of the disk [18]. The accumulated plastic deformation and dynamic recrystallization lead to uniform strain distribution, finally resulting in a more refined and homogeneous microstructure according to the homogeneous microhardness result.

Also, Fig. 3b and Table 2 show the density of the samples at each condition measured using the Archimedes method. The relative density compared to the wrought specimen is ~93.6% just after pre-compaction, ~98.7% after the HPT process by 1 turn, and finally reached ~99.6% after 4 turns, which surpasses the relative density values of 316L stainless steel processed by other PM techniques [3,19].

Fig. 4 displays SEM - SE micrographs of the central regions of the as-HPT samples subjected to 1, 2, and 4 turns of the HPT. In the sample subjected to 1 turn, pores align with powder boundaries and concentrate at junctions between powder particles. This distribution is attributed to the lower strains of the 1-turn HPT process. As the number of HPT turns increases, pores diminish, leading to a more consolidated microstructure, achieving full density in the as-HPT sample with 4 turns.

Table 2
Relative densities of each step during the powder cold-consolidation and annealing using high-pressure torsion.

Process	Measured density, g/cm^3	Relative density, %
Pre-compacted	7.47 ± 0.22	93.6 ± 2.8
HPT processed (1 turn)	7.78 ± 0.17	97.4 ± 1.5
HPT processed (4 turns)	7.95 ± 0.03	99.6 ± 0.3
Theoretical density	7.98	100

3.2. Microstructural characterization and phase evolution after post-HPT annealing

The EBSD-inverse pole figure (IPF), corresponding image quality (IQ) overlapping with the grain and coincidence site lattice (CSL, Σ 3~ Σ 11) boundaries, Kernal average misorientation (KAM), and IPF texture maps of the annealed samples are demonstrated in Fig. 5a–d. It is observed that the average grain size increases from ~709 nm in the A700-15 sample to ~1.39 μm in the A800-60 sample as the annealing time and temperature increase. Also, the nanocrystalline grains induced

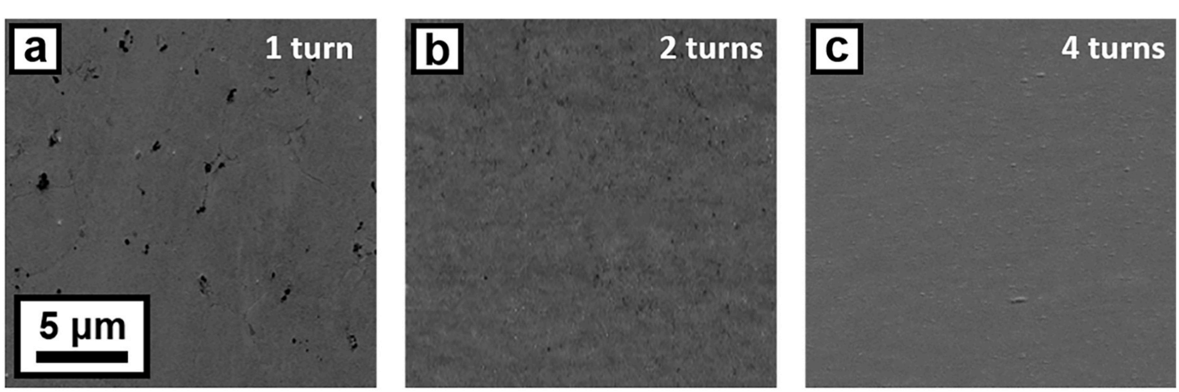

Fig. 4. SEM - SE images of center areas of the as-HPT samples with (a) 1, (b) 2, and (c) 4 turns of HPT.

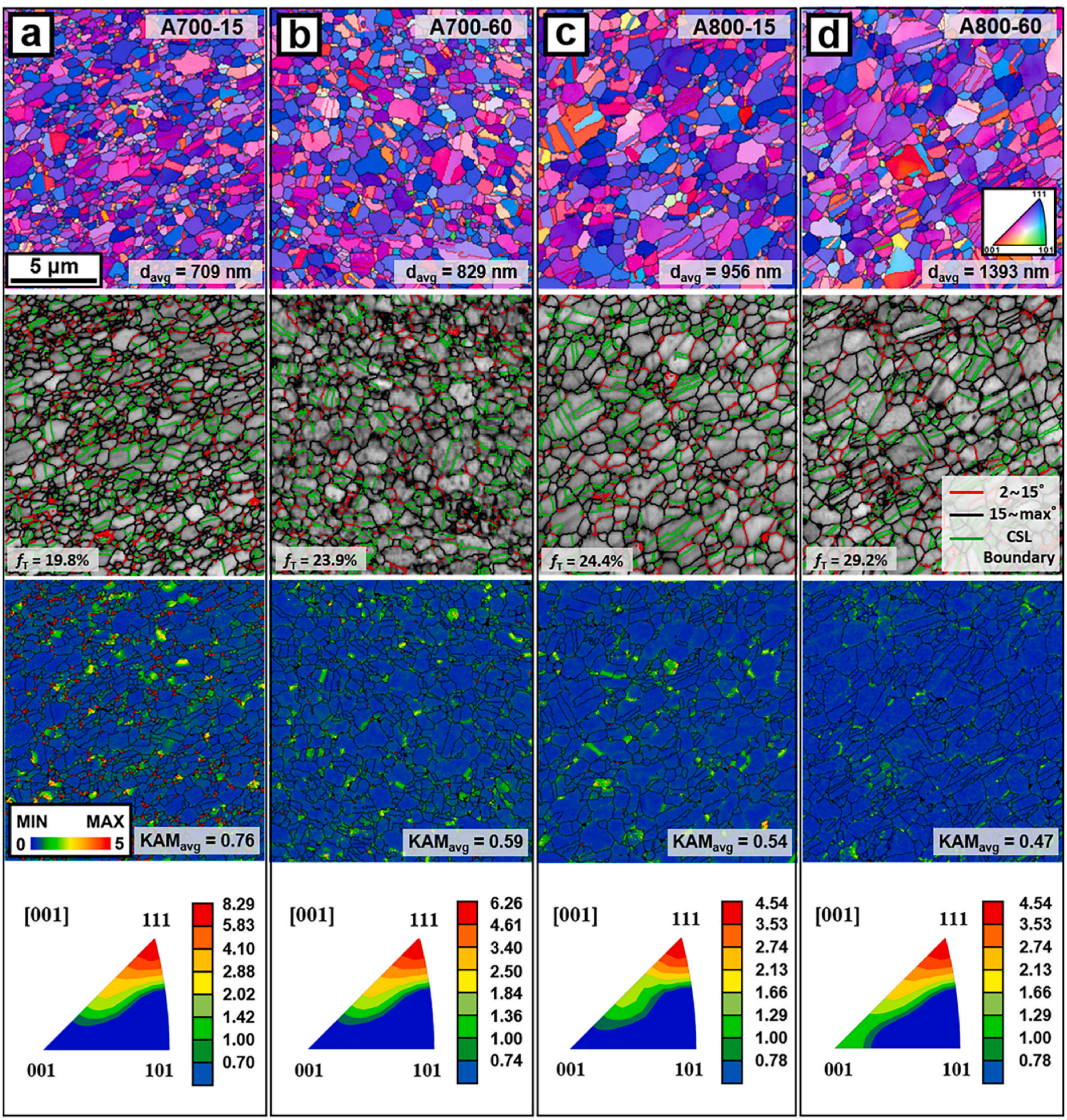

Fig. 5. EBSD inverse pole figure (IPF) maps, image quality (IQ) maps with LAGB in red lines, HAGB in black lines, and CSL boundary (Σ3∼ Σ11) in green lines, Kernal average misorientation (KAM) maps and IPF textures of the (a) A700-15, (b) A700-60, (c) A800-15, and (d) A800-60 samples. The fraction of average grain sizes (d_{avg}), annealing twins (f_T), and average KAM value (KAM_{avg}) are displayed for each microstructure. (For interpretation of the references to color in this figure legend, the reader is referred to the Web version of this article.)

by HPT and the enlarged grains with some annealing twins are properly distributed in the microstructure after post-HPT annealing. The low-angle grain boundaries (LAGB) with the misorientation angle of less than 15°, and high-angle grain boundaries (HAGB) with that of higher than 15° are indicated with red, and black lines, respectively. In all post-HPT annealed samples, the fraction of annealing twins (f_T) identified as CSL boundaries, which are marked in green lines, increases with higher annealing temperatures or prolonged annealing times, showing a direct correlation between the degree of recrystallization and annealing conditions. The corresponding KAM maps of the post-HPT annealed samples display measurements up to the third nearest neighbor Kernel with a maximum misorientation of 5°. All the annealed samples have an average KAM value below 1°. Geometrical necessary dislocations (GND) tend to accumulate at boundaries between recrystallized and nano-crystalline grains. However, as annealing time or temperature increases, the average KAM value decreases due to a reduced GND density and an

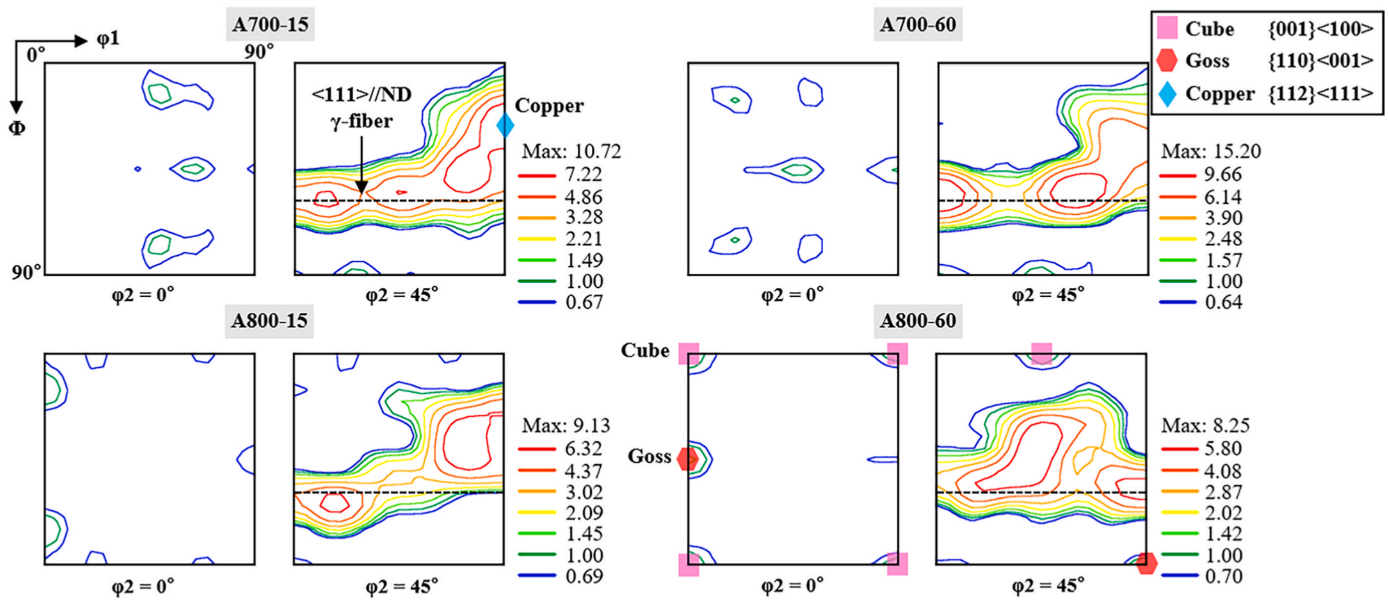

Fig. 6. Textures of the post-HPT annealed samples represented by $\varphi_2 = 0°$, and 45° orientation distribution function (ODF) sections, derived from EBSD texture measurements. These textures originated from typical rolled components of FCC alloys.

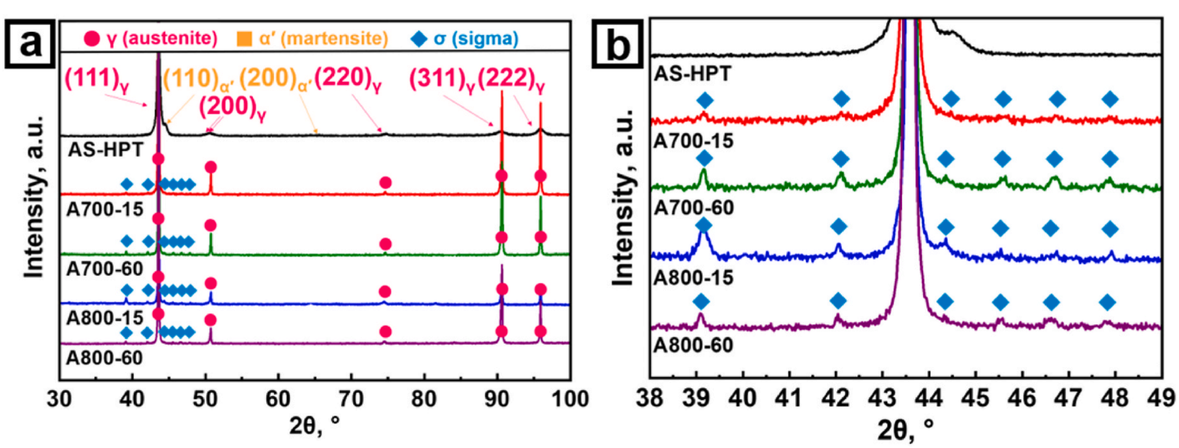

Fig. 7. (a) XRD patterns of the as-HPT sample and the post-HPT annealed samples under various conditions, (b) Magnified XRD patterns of (a) in the 2θ range of 38°–49°.

Table 3
Peak index used on the calculation and the dislocation densities of the as-HPT and annealed samples through the CMWP method based on the XLPA results.

Sample	2 theta					Index					Dislocation density, m^{-2}
AS-HPT	43.60	50.57	74.66	90.47	95.89	(111)	(200)	(220)	(311)	(222)	6.42×10^{15}
A700-15											9.37×10^{14}
A700-60											1.25×10^{14}
A800-15											1.11×10^{14}
A800-60											7.64×10^{13}

increase in grain size [20]. Fig. 6 demonstrates the textures of the post-HPT annealed samples as represented by orientation distribution function (ODF) maps at $\varphi_2 = 0°$, and 45° sections. The initial microstructures of all the annealed samples basically show strong intensities along the deformation texture components of γ-Fiber with Copper texture featured typically in severely deformed FCC structures. These textures tend to shift to Cube and Goss textures, revealing weak intensity at $\varphi_2 = 0°$, indicative of the typical annealed texture during recrystallization in the post-HPT annealing process [21,22].

The XRD patterns of the as-HPT and the post-HPT annealed samples are shown in Fig. 7a. The XRD patterns present body-centered cubic (BCC) α′-martensite peaks in the as-HPT sample, confirming the strain-induced martensitic transformation during HPT [23]. The combination of high pressure and shear strain imposed by HPT leads to the reorientation of the crystal structure, resulting in the formation of α′-martensite. However, the BCC peaks are not detected in the post-HPT annealed samples, indicating that the reverse phase transformation from BCC to FCC occurs during the post-HPT annealing [8,9]. The heat treatment provides the activation energy for atomic rearrangement and diffusion, allowing the material to revert back its original austenitic phase. On the other hand, there are minor secondary peaks in all annealed samples intensively from 38° to 49°, which could be related to the σ phase (Fig. 7b) [24,25]. It can be deduced from the results previously reported about the typical σ phase formation in heat-treated 316L stainless steels in the temperature range of 600–900 °C [26–28]. Furthermore, the TTT curve was plotted using ThermoCalC software to elucidate the sigma phase evolution of 316L stainless steel in this research, confirming that the sigma phase precipitation occurs at 700–800 °C (Fig. S1).

The dislocation densities in the austenite phase of the as-HPT and post-HPT annealed samples are calculated by the CMWP method from the XLPA results, as shown in Table 3. The post-HPT annealing decreases the dislocation density from 6.42×10^{15} m^{-2} in the as-HPT condition. The dislocation density of A800-60 (7.64×10^{13} m^{-2}) is much lower than that of the as-HPT sample, due to reduced opportunities for GND emission from grain boundaries during post-HPT annealing.

3.3. Tensile properties

The mechanical properties of the as-HPT and samples annealed at each condition are illustrated in Fig. 8a. The as-HPT sample reaches the superior yield strength of ~1.85 GPa with total elongation of ~15.8% (Table 4). For the as-HPT and A700-15 samples, strain softening is observed at the early onset of necking. This phenomenon is attributed to dislocation creation and absorption at grain boundaries, often observed in nanocrystalline alloys fabricated by SPD [29]. The as-HPT and A700-15 sample exhibit a significant reduction in ductility, attributed to substantial dislocation density with ultrafine grained (UFG) microstructures. This reduction is primarily due to early plastic instability driven by their high yield strength and limited strain-hardening capacity. However, it is known that post-HPT annealing induces the annihilation of dense dislocations and grain growth with increased time and temperature [17,18,29]. These factors contribute to reduced HPT-induced dislocations, leading to enhanced strain-hardening capacity. Conversely, the evolution of incoherent precipitates within the matrix results in a limited strain-hardening capacity, as these precipitates cannot effectively block or generate dislocations over prolonged straining. The interplay between dislocation density annihilation and precipitation evolution influences the ductility of the post-HPT annealed samples. Therefore, a strength-ductility trade-off is evident in the post-HPT annealed samples, with enhanced ductility being primarily governed by dislocation annihilation and alleviated precipitation at elevated temperatures and/or longer durations. Especially, the A700-60 sample is estimated to have a remarkable result of yield strength of ~1 GPa with total elongation of ~46%. Fig. 8b illustrates the strain hardening rate (SHR) with corresponding true stress-strain curves. For the as-HPT and annealed samples, the SHR curves initially drop drastically, which could be related to the yield drop phenomenon usually observed in UFG materials caused by discontinuous yielding [30–33]. Then, the SHR curves of the A700–60, A800-15, and A800-60 samples increase with strain and reach relatively constant values until the onset of plastic instability. These plateau ranges are induced mainly by restrained movement of dislocations locked around densified grain boundaries and nano-scale precipitates in grain interior [34,35]. The SHR curve of these samples decreases after reaching ultimate tensile strength due to plastic instability of materials.

Table 4
Tensile properties, including yield strength (YS), ultimate tensile strength (UTS), total elongation (T. El), and uniform elongation (U. El) of each sample.

Process	YS , MPa	UTS, MPa	T. El, %	U. El, %
AS-HPT	1850 ± 29	1889 ± 42	15.8 ± 0.4	3.6 ± 0.5
A700-15	1260 ± 11	1260 ± 7	28.5 ± 1.2	1.7 ± 0.3
A700-60	995 ± 8	1085 ± 15	44.8 ± 0.5	25.0 ± 1.7
A800-15	843 ± 15	957 ± 9	45.1 ± 1.4	27.9 ± 1.9
A800-60	688 ± 13	818 ± 17	68.8 ± 1.8	35.6 ± 2.5

Fig. 9 demonstrates the microstructural analysis of the A700-60 sample at local strains of ~15% (at the middle of the plastic region) and ~25% (at the region close to the onset of necking). The grains are elongated, and mechanical twins are not identified while the true strain increases, as illustrated in the EBSD-IPF maps. The corresponding Kernel average misorientation (KAM) maps at two strain levels demonstrate the accumulation of dislocation into the lattice during plastic deformation. The average KAM values are increased with the increment of the local strain from 0.87 to 0.92, indicating that the dislocation gliding mechanism predominantly governs the plastic deformation in this sample. It means that the increase in the KAM value indicates an increase in local misorientation of the lattice due to dislocation accumulation. Finally, the nanocrystalline structure and nano-scale σ precipitates in the A700-60 sample play a pivotal role in activating dislocations during tensile testing, which is crucial for the enhanced elongation of the sample. This mechanism includes the hindrance of dislocation movement, predominantly through Orowan looping around the precipitates and the accumulation of dislocations at grain boundaries. Also, it significantly influences the development of stacking faults and nano-twins, thereby greatly enhancing the ductility observed in the A700-60 sample [8,36].

The yield strength and total elongation of the present samples are compared with the other PM-processed 316L stainless steels in Fig. 10 and Table S1. The present study exhibits superior yield strength and total elongation compared to the other conventional PM techniques. The advantages are particularly noticeable in cases such as A700–15, A700-60, and A800-15, especially when compared to research involving bulk-HPT annealed materials. The present outstanding tensile properties originate from the novel powder cold-consolidation and annealing that induces the utmost densification, nano/ultrafine-grained microstructure, substantial dislocation densities, and nano-scaled precipitates.

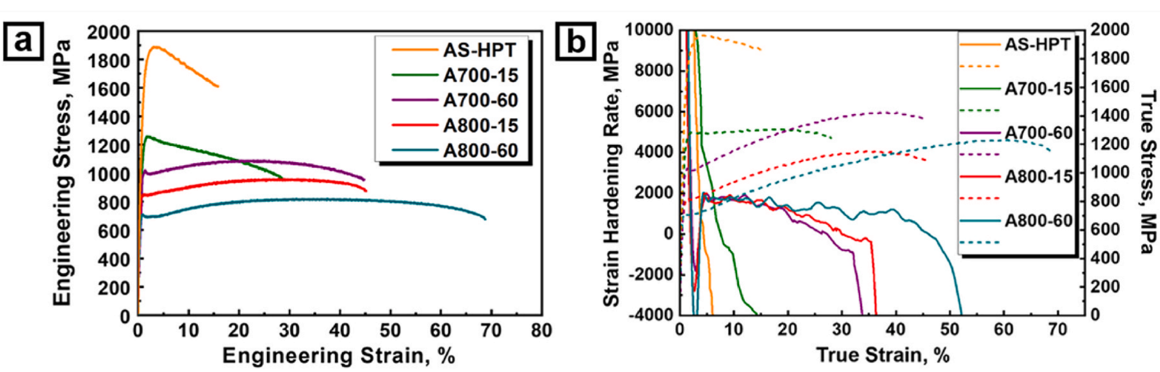

Fig. 8. (a) Engineering stress-strain curves of the tensile test for the as-HPT and post-HPT annealed samples, and (b) corresponding true stress-strain curves (dash-line) and strain hardening rate-true strain curves of the as-HPT and post-HPT annealed samples.

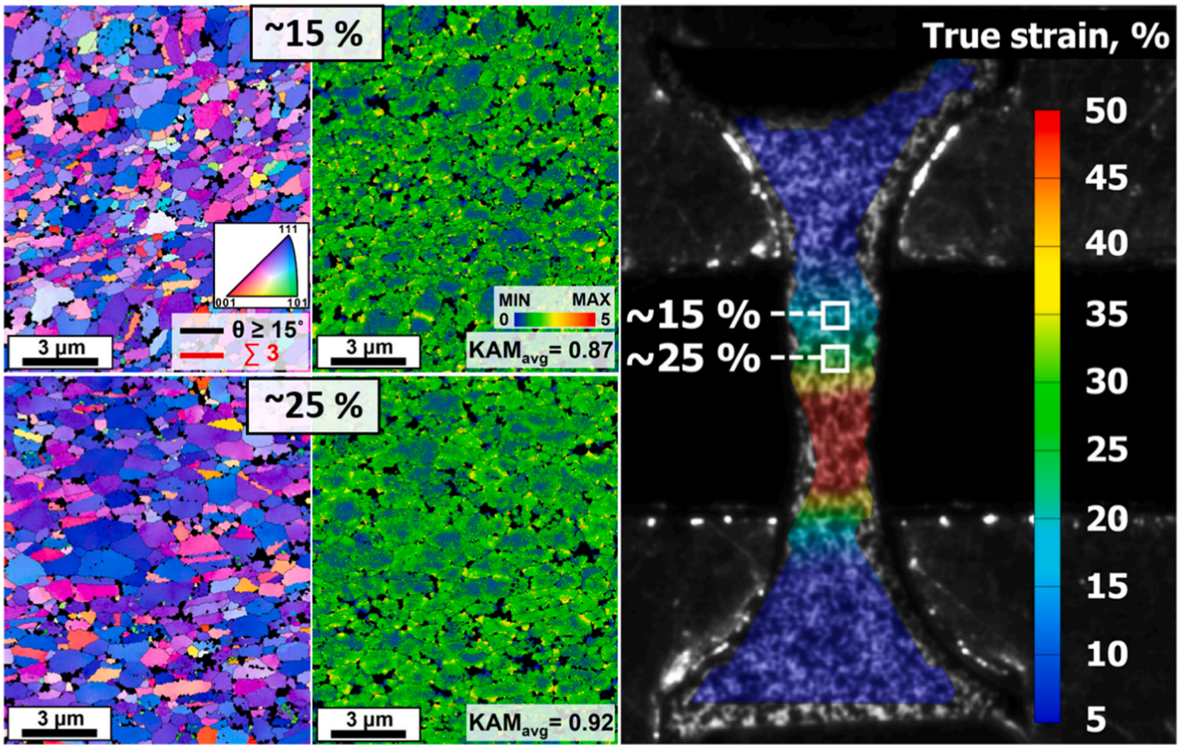

Fig. 9. Major strain distribution map of the A700-60 sample direct before the fracture during the tensile test and EBSD-IPF and corresponding KAM maps at two different local strains of ~15% and ~25%.

3.4. Elements segregation and precipitates evolution in A700-60

It is necessary to conduct a thorough microstructural investigation about A700-60 sample which has the excellent combination of strength-ductility beyond the grain refinement strengthening. Fig. 11a shows the BSE image of A700-60 that features subgrain-sized precipitates in the junction of grain boundaries around the FCC matrix. Elemental distribution analysis using line-scanned EDS accurately shows an abundance of Cr and Mo, while Fe and Ni are depleted in the marked area along the precipitate (Fig. 11b). It demonstrates that the Cr and Mo segregated precipitates form in the energetically unstable areas such as the grain boundaries during the post-HPT annealing.

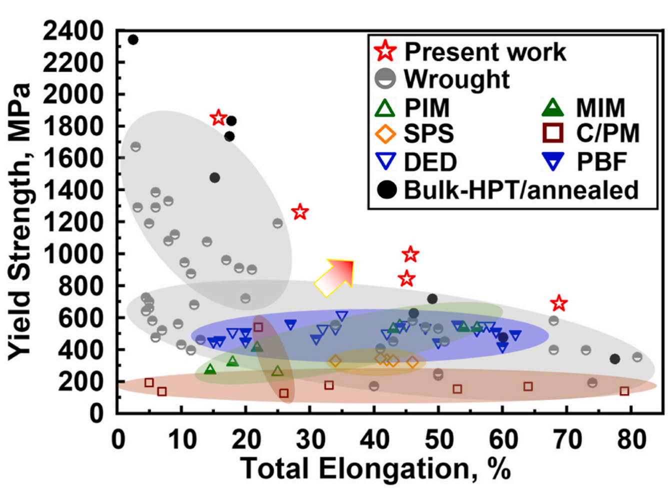

Fig. 10. Comparison of yield strength vs. total engineering elongation of the present work with other 316L stainless steels processed by other PM techniques such as conventional PM (C/PM) which includes a uniaxial press and sintering, PIM, MIM, SPS, additive manufacturing processed by direct energy deposition (DED) and powder bed fusion (PBF), wrought materials, and bulk materials processed by HPT and post-annealing (Bulk-HPT/annealed). The tensile properties of each reference of 316L stainless steel are listed in Table S1.

The BF-TEM image of the A700-60 sample is specifically displayed about the microstructures in Fig. 12a. The annealed microstructure consists of equiaxed grains with two different types of precipitates. The dark precipitates with equiaxed morphology can be seen in the grain boundaries, and the black dot precipitates can be found in the grain interiors. To certify the formation of the Cr and Mo segregation in the black dot precipitates, a map scanning on the selected area of the BF-TEM image in Fig. 12a is conducted using TEM-EDS (Fig. 12b). The EDS results of the selected area of A700-60 sample show that fine-equiaxed precipitates dispersed in the grain interior as well as along the grain boundaries exhibit Cr- and Mo-segregated distribution in the region with the precipitates.

These two types of precipitates take on different sizes throughout the microstructures due to the different nucleation mechanisms. The precipitates formed along the grain boundaries show a relatively coarse (RC) size of about 150~300 nm (Fig. 13a). Fig. 13a also exhibits the emergence of RC precipitates between the deformed and recrystallized areas, and the accumulation of dislocations around their boundaries in the A700-60 sample (Fig. 13a$_2$). Fig. 13b illustrates the SAED pattern from one of the RC precipitates presented in Fig. 13a, indicating that the RC precipitate consists of the body-centered tetragonal (BCT) structure with a [110] zone axis known as σ phase in stainless steels [37]. On the other hand, the precipitates nucleated in the grain interior are relatively fine (RF) with a size of about 20~60 nm (Fig. 13c). The SAED pattern from the RF precipitates indicates the BCT structure with a [410] zone axis, demonstrating the feasibility of segregation and nucleation of the σ phase in a lower energy region, such as grain interior and subgrain boundaries (Fig. 13d). Fig. 14 depicts the hindrance of dislocation accumulation by nano-sized precipitates and at segregation sites such as grain boundaries, preventing dislocation annihilation during annealing and maintaining residual dislocations. These precipitates and segregation sites result in higher dislocation densities even after post-HPT annealing.

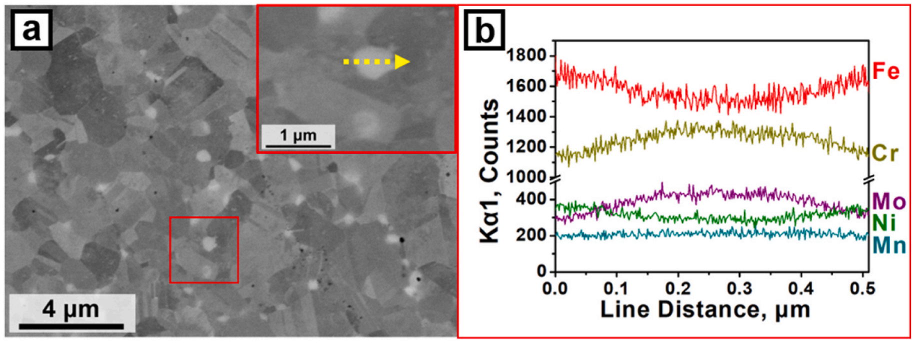

Fig. 11. (a) BSE image with (b) an EDS line scanning from a precipitate marked with lines along the direction.

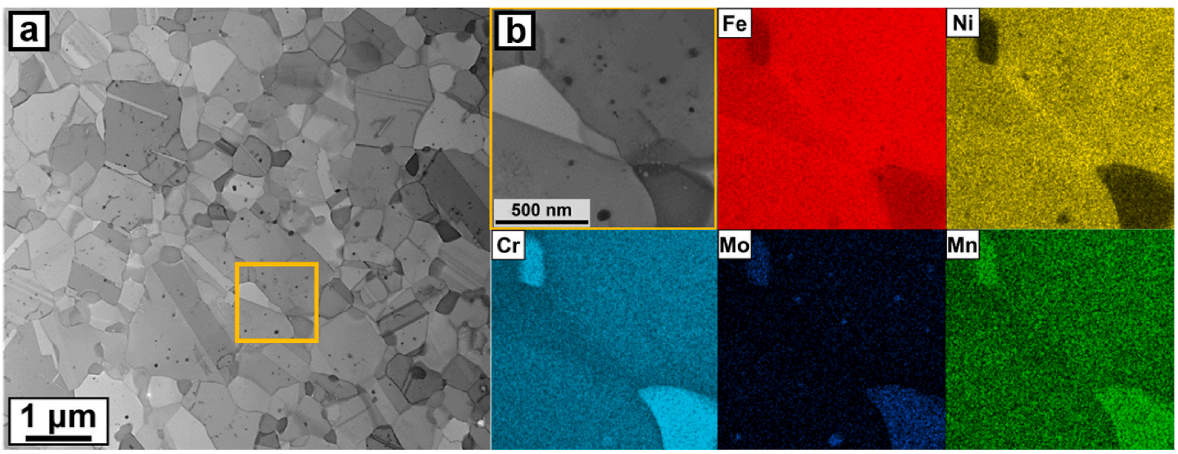

Fig. 12. (a) BF-TEM image with yellow-colored marked area of the A700-60 sample, and (b) TEM-EDS maps of the A700-60 sample from the marked area in (a). (For interpretation of the references to color in this figure legend, the reader is referred to the Web version of this article.)

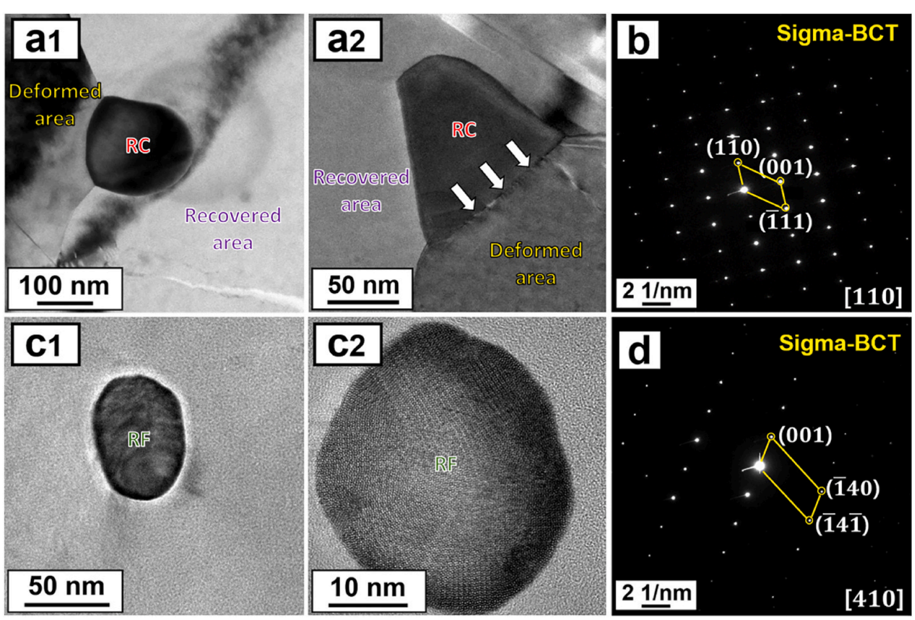

Fig. 13. High resolution (HR)-TEM images of RC precipitates (a1, a2) at the junction of grain boundaries in the A700-60 sample with (b) the corresponding SAED patterns, and HR-TEM images of RF precipitates (b1, b2) in the interior of grain in the A700-60 sample with (d) the corresponding SAED patterns.

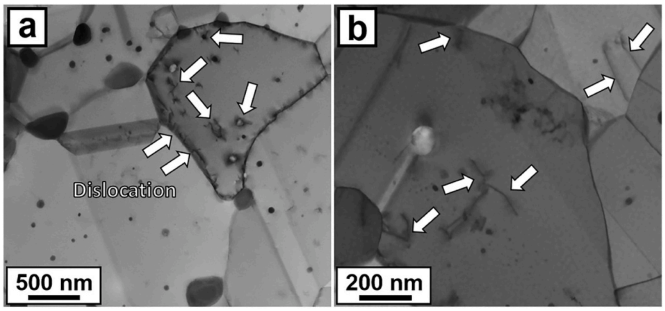

Fig. 14. HR-TEM images showing the dislocation accumulation (White arrows) of the A700-60 sample hindered by the RF precipitates and at the segregation boundaries such as grain boundaries.

4. Discussion

4.1. σ phase evolution during post-HPT annealing

The severely deformed nanocrystalline structure of as-HPT includes α′-martensite formed by strain-induced martensitic transformation, as observed in XRD results in Figs. 6a and 15a. Further, it exhibits the metastable phase around the FCC matrix that has a high dislocation density and nano-twin, contributing to the increase of residual stresses. This feature shows promising potential during post-HPT annealing for metastable phase transformation by element segregation, and reverse austenitic transformation which induces the relief of dislocation and residual stresses [8,9]. Indeed, it can be observed that post-HPT annealing removes α′-martensite as evident in Fig. 6a, and reduces the dislocation densities from 6.42×10^{15} to 1.25×10^{14} m^{-2}, as plotted and calculated by the CMWP method from the XLPA results. However, due to remaining the unclarity of the nucleation and growth mechanism of secondary σ phases, Fig. 15 manifests the mechanism of evolution of nano-scale σ precipitates in two different types of size.

It is inferred from TEM image in Fig. 13 that the two different sizes of σ nano-precipitates has been observed after post-HPT annealing. In the case of RC precipitates, the sources of nucleation and growth are almost generated along the phase boundaries between α′-martensite and austenitic FCC matrix, also with grain boundaries, and in the junctions of grain boundaries [27,38]. The significant reason for such precipitation at the energetically metastable sites is element segregation. The accelerated diffusion of Cr and Mo in severely-deformed FCC regions could contribute to the diffusion and partition around the grain boundaries (Fig. 15b) [39]. Furthermore, Fig. 5b shows the formation of recrystallized grains through heat treatment, and the boundaries between these recrystallized grains and the non-recrystallized areas also play a role in inducing the grain boundary segregation of Cr and Mo as observed in Fig. 13a (Fig. 15c) [37]. These elements stimulate to the σ phase nucleation, and the crystallographic growth either along with the direction of recrystallization or in the direction of reduced residual stress (Fig. 15d and e). As a result, it can be deduced that the RC precipitates have formed on the final microstructure of the A700-60 sample.

On the other hand, the relatively smaller RF precipitates can be observed to form at the sites where precipitation is mostly inhibited, such as within the crystal lattice. The reason of Cr and Mo segregation, which promotes the evolution of RF nano-scale precipitates, can be speculated from the microstructure of as-HPT. The metastable α′-martensite and severely-deformed areas in as-HPT samples have crucial impacts on the RF precipitation. Lath or plate martensite in severely-deformed FCC structure forms have a significant influence on Cr and Mo diffusion at the moment of initial heat treatment. The diffusion rate of both Cr and Mo is over 100 times faster in BCC structure than in FCC structure [26]. Thus, as martensite undergoes reverse austenitic transformation via diminishing the size of the martensite, Cr and Mo actively diffuse and segregate, leading to the transformation of BCC α′-martensite into BCT σ phase (Fig. 15b and c). Also, the severely-deformed areas can generate a compressive stress field due to the high dislocation density [37]. These compressive stress fields within the nanocrystalline FCC matrix suppress the growth of nucleated σ phase at the early stage of the heat treatment, even as the heat treatment progresses (Fig. 15d and e). Therefore, the RF precipitates are established within the grain interior on the A700-60 sample. This precipitation mechanism driven by post-HPT annealing is frequently reported in various studies; Ag segregation from a supersaturated Cu matrix in a Cu–Ag–Zr alloy [40], precipitation of NiMn-, Cr-, and FeCo-rich phases along the grain boundaries and interior [41], and carbide precipitation at the boundaries of lamellar structures in low-carbon steel [42].

Both types of nano-scale σ precipitates have a significant lattice misfit with the FCC matrix and constitute a non-negligible fraction of inter-particle spacing, also with an area fraction of approximately 6.8% within the nano-scale microstructure (Fig. 12a). This indicates that the precipitates can interact with dislocations and hinder their movement, leading to suggest Orowan mechanism caused by the precipitates [43,44]. Hence, these σ precipitates can lead to an increase in yield strength due to the precipitation strengthening through the Orowan mechanism. This can also result in strain hardening, which should be further investigated through detailed analysis of the deformed microstructure.

4.2. The contribution of strengthening mechanism on yield strength of A700-60

The A700-60 sample shows excellent tensile properties with high ductility due to adequate work hardening while maintaining high yield strength. The yield strength of the A700-60 (σ_y) can be attributed to the aggregation of grain boundary strengthening, dislocation strengthening and precipitation strengthening. Consistently, these contributions can be expressed as follows:

$$\sigma_y = \sigma_0 + \sigma_{gb} + \sigma_{dis} + \sigma_{ppt} \quad (1)$$

where σ_0 is the lattice-friction stress (~169 MPa, Tables 5 and 6), σ_{gb}, σ_{dis}, and σ_{ppt} respectively terms of the stress contribution from the grain size refinement, the dislocation density, and the precipitation strengthening effects of the A700-60 sample [45]. The equations of each yield strengthening mechanism in the A700-60 sample are presented in Table 5, and the reference coefficients of the quantification in the A700-60 sample, which are related to standard 316L stainless steel, are explicitly stated in Table 6. Grain boundary strengthening arises due to the impediment of dislocation motion by grain boundaries. Smaller grains mean more boundaries, which hinder dislocation movement more effectively. The σ_{gb} is calculated as ~406 MPa by substituting the average grain size of ~829 nm using the data in Fig. 5b. Dislocation strengthening (σ_{dis}), driven by the density and interaction of dislocations within the material, contributes ~176 MPa through the result of the dislocation densities of 1.25×10^{14} m^{-2} from the XLPA using the CMWP analysis. Also, the hard precipitates with BCT σ phase can induce the interaction with the dislocation by bowing around the precipitates or shearing the precipitates, leading to the Orowan mechanism [46,47]. It can be quantified with the Orowan mechanism that the σ_{ppt} account for ~217 MPa by substituting the average precipitate diameter of ~72 nm and the average precipitate fraction of ~6.8% from the BF-TEM image in Fig. 12a. These values account for approximately 22% of the yield strength, allowing us to quantitatively conclude that the precipitation strengthening effect in this alloy has a significant impact on the increase in yield strength. In the current study, texture strengthening, due to the preferred grain orientation of A700–60, has not been inherently reflected in the contribution of strengthening mechanisms. The calculated Taylor factor of approximately 3.16, indicative of the pronounced texture orientation as a developed slip system of the deformed FCC matrix, subtly influences dislocation strengthening and precipitate

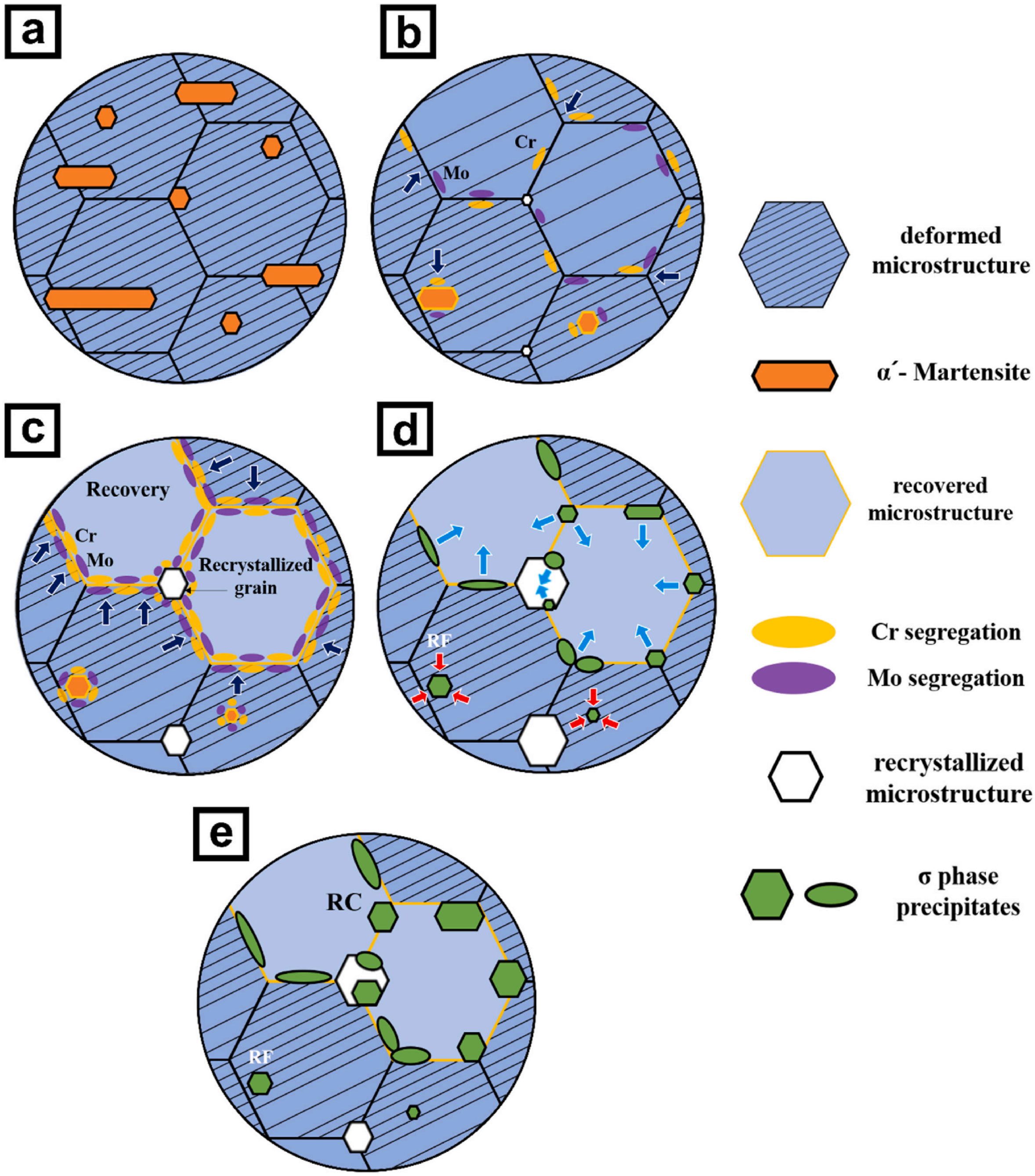

Fig. 15. Schematic representation of the evolution and growth mechanism of nano-scale σ precipitates in the A700-60 sample during post-HPT annealing. (a) Strain-induced martensitic transformation in the nanocrystalline structure, highlighting the formation of α′-martensite; (b) element segregation at energetically metastable sites, especially along phase boundaries and grain boundaries, with rapid diffusion of Cr and Mo in severely-deformed FCC regions; (c) induction of grain boundary segregation of Cr and Mo due to the formation of boundaries between recrystallized and non-recrystallized areas; (d) nucleation and directional growth of σ phase, either along the direction of recrystallization or towards areas with reduced residual stress, leading to (e) the formation of larger RC precipitates and smaller RF precipitates within the grain interior, influenced by the metastable α′-martensite and severely deformed regions.

Table 5
Equations of each strengthening mechanism contributed to the yield strength of the A700-60 sample [48].

Strengthening mechanism	Equation	Equation number
Lattice friction stress (σ_0)	σ_0	–
Grain boundary strengthening (σ_{gb})	$\sigma_{gb} = k \bullet D^{-1/2}$	(2)
Dislocation strengthening (σ_{dis})	$\sigma_{dis} = M\alpha G b \rho^{1/2}$	(3)
Precipitation strengthening (σ_{ppt})	$\sigma_{ppt} = M\frac{0.4Gb}{\pi\lambda}\frac{\ln(2\bar{r}/b)}{\sqrt{1-\nu}}$	(4)
	$\lambda = 2\bar{r}\left(\sqrt{\frac{\pi}{4f}}-1\right)$	(5)
	$\bar{r} = \sqrt{\frac{2}{3}}r$	(6)

Table 6
Reference coefficients of 316L stainless steel on the equations in Table 5.

Coefficient	Definition	Unit	Values	Reference
σ_0	Lattice friction stress	*MPa*	169.15	[49]
k	Hall-Petch coefficient	$MPa \bullet m^{1/2}$	0.37	[50]
D	Average grain size	*nm*	829	Present
M	Taylor factor	–	3.16	Present
α	Constant for FCC metals	–	0.24	[51,52]
G	Shear modulus	*GPa*	82	[53]
b	Burger's vector	*nm*	0.254	[54,55]
ρ	Dislocation density	m^{-2}	$1.25 \bullet 10^{14}$	Present
λ	Edge to edge inter-precipitates spacing	*nm*	283.14	Calculated
$\bar{r}$	Mean radius of a circular cross-section in a random plane	*nm*	58.85	Calculated
ν	Poisson's ratio	–	0.3	[56]
f	Volume fraction	%	6.77	Present
r	Mean radius of the precipitates	*nm*	72.08	Present

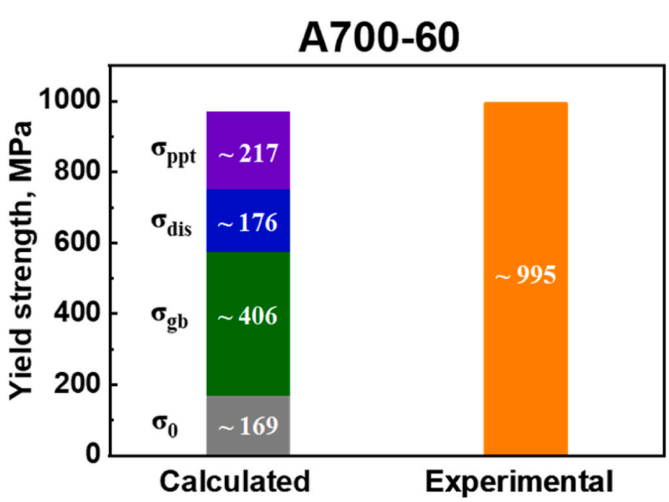

Fig. 16. Bar graph of each calculated strengthening contribution and experimental yield strength of the A700-60 sample.

strengthening.

Fig. 16 displays the bar graph to compare the experimental data with the calculated data for the yield strength of the A700-60 sample composed of the contribution of each strengthening mechanism. The calculated yield strength of ~969 MPa is approximately correlated with the calculated yield strength of ~995 MPa, which induces that these three types of strengthening mechanisms contribute to the yielding of the processed materials.

5. Conclusion

In this study, 316L stainless steel powder has been processed by the cold-consolidation technique using HPT process and post-HPT annealing. The main discoveries and conclusions are summarized as follows.

(1) Present cold-consolidation route redeems the processing-related disadvantages of the PM, such as pores, by displaying enhanced densification deduced from the severe HPT-induced strain. The prosperous annealing enlarges the uniform elongation by the recovery of the HPT-induced dislocations and persuades the segregation of certain elements, leading to precipitation.
(2) Combination of novel powder metallurgy techniques and post-HPT annealing can improve the densification and microstructure of 316L stainless steel, leading to enhanced tensile properties. In particular, A700-60 sample demonstrates an impressive yield strength of approximately 1 GPa, accompanied by a remarkable total elongation of around 46%.
(3) The formation of nano-scale σ precipitates during post-HPT annealing retard the grain growth during post-HPT annealing, and suppress the dislocation motion during tensile deformation, contributing to the additional strengthening.
(4) The strengthening mechanisms induced by grain boundaries, dislocations and precipitates significantly contribute to the yield strength of the A700-60 sample. Specifically, precipitation strengthening has a substantial impact on the increase in strength.
(5) These achievements as a breakthrough in the PM authenticate the feasibility of utilizing the present fabrication technique to overcome the tensile strength-ductility dilemma in the PM.

CRediT authorship contribution statement

Do Won Lee: Writing – review & editing, Writing – original draft, Visualization, Methodology, Investigation, Data curation, Conceptualization. **Peyman Asghari-Rad:** Writing – review & editing, Investigation, Conceptualization. **Yoon-Uk Heo:** Supervision, Investigation, Data curation. **Sujung Son:** Supervision, Data curation. **Hyojin Park:** Visualization, Investigation. **Ji-Su Lee:** Visualization, Data curation. **Jae-il Jang:** Validation, Supervision. **Byeong-Joo Lee:** Validation, Supervision. **Hyoung Seop Kim:** Writing – review & editing, Supervision, Project administration, Methodology, Investigation, Funding acquisition, Conceptualization.

Declaration of competing interest

The authors declare that they have no known competing financial interests or personal relationships that could have appeared to influence the work reported in this paper.

Data availability

Data will be made available on request.

Acknowledgment

This research was supported by the National Research Foundation of Korea (NRF) grant funded by the Korean government (MSIP) (NRF-2021R1A2C3006662) and (NRF-2022R1A5A1030054).

Appendix A. Supplementary data

Supplementary data to this article can be found online at https://doi.org/10.1016/j.msea.2024.146107.

References

[1] R.K. Desu, H.N. Krishnamurthy, A. Balu, A.K. Gupta, S.K. Singh, Mechanical properties of austenitic stainless steel 304L and 316L at elevated temperatures, J. Mater. Res. Technol. 5 (2016) 13–20, https://doi.org/10.1016/j.jmrt.2015.04.001.

[2] S. Basak, S.K. Sharma, M. Mondal, K.K. Sahu, S. Gollapudi, J.D. Majumdar, S. T. Hong, Electron beam surface treatment of 316L austenitic stainless steel: improvements in hardness, wear, and corrosion resistance, Met. Mater. Int. 27 (2021) 953–961, https://doi.org/10.1007/s12540-020-00773-y.

[3] K. Chadha, Y. Tian, J. Spray, C. Aranas, Microtextural characterization of additively manufactured SS316L after hot isostatic pressing heat treatment, Met. Mater. Int. 28 (2022) 237–249, https://doi.org/10.1007/s12540-021-01046-y.

[4] A. Basir, A.B. Sulong, N.H. Jamadon, N. Muhamad, U.B. Emeka, Process parameters used in macro/micro powder injection molding: an overview, Met. Mater. Int. 27 (2022) 2023–2045, https://doi.org/10.1007/s12540-020-00767-w.

[5] J. Lu, Q. Wang, C. Liu, C. Zhang, D. Chen, G. Cui, Cracking behavior of AISI 316L stainless steel powder by gas nitriding and its influence on spark plasma sintering, J. Mater. Res. Technol. 20 (2022) 3796–3806, https://doi.org/10.1016/j.jmrt.2022.08.163.

[6] F. Bartolomeu, M. Buciumeanu, E. Pinto, N. Alves, O. Carvalho, F.S. Silva, G. Miranda, 316L stainless steel mechanical and tribological behavior-A comparison between selective laser melting, hot pressing and conventional casting, Addit. Manuf. 16 (2017) 81–89, https://doi.org/10.1016/j.addma.2017.05.007.

[7] C. Suryanarayana, Mechanical alloying and milling, Prog. Mater. Sci. 46 (2001) 1–184, https://doi.org/10.1016/S0079-6425(99)00010-9.

[8] P. Asghari-Rad, P. Sathiyamoorthi, N.T.-C. Nguyen, A. Zargaran, T.S. Kim, H. S. Kim, A powder-metallurgy-based fabrication route towards achieving high tensile strength with ultra-high ductility in high-entropy alloy, Scripta Mater. 190 (2021) 69–74, https://doi.org/10.1016/j.scriptamat.2020.08.038.

[9] S. Son, P. Asghari-Rad, A. Zargaran, W. Chen, H.S. Kim, Superlative room temperature and cryogenic tensile properties of nanostructured CoCrFeNi medium-entropy alloy fabricated by powder high-pressure torsion, Scripta Mater. 213 (2022) 114631, https://doi.org/10.1016/j.scriptamat.2022.114631.

[10] G.M. Karthik, P. Asghari-Rad, P. Sathiyamoorthi, A. Zargaran, E.S. Kim, H.S. Kim, Architectured multi-metal CoCrFEMnNi Inconel 718 lamellar composite by high-pressure torsion, Scripta Mater. 195 (2021) 113722, https://doi.org/10.1016/j.scriptamat.2021.113722.

[11] P. Asghari-Rad, N.T.-C. Nguyen, Y. Kim, A. Zargaran, P. Sathiyamoorthi, H.S. Kim, TiC-reinforced CoCrFeMnNi composite processed by cold-consolidation and subsequent annealing, Mater. Lett. 303 (2021) 130503, https://doi.org/10.1016/j.matlet.2021.130503.

[12] P. Asghari-Rad, Y.T. Choi, N.T.-C. Nguyen, P. Sathiyamoorthi, H.S. Kim, Fabrication of layered Cu-Fe-Cu structure by cold consolidation of powders using high-pressure torsion, J. Powder Mater. 28 (2021) 287–292, https://doi.org/10.4150/KPMI.2021.28.4.287.

[13] G.H. Gu, Y.U. Heo, H. Kwon, S.Y. Ahn, S. Son, P. Asghari-Rad, H.S. Kim, Synergy of tensile strength-ductility in IN718/CoCrFeMnNi/IN718 multi-material processed by powder high-pressure torsion and annealing, Scripta Mater. 225 (2023) 115167, https://doi.org/10.1016/j.scriptamat.2022.115167.

[14] R. Wang, Precipitation of σ phase in duplex stainless steel and recent development on its detection by electrochemical potentiokinetic reactivation: a review, Corros. Comms. 2 (2021) 41–54, https://doi.org/10.1016/j.corcom.2021.08.001.

[15] V.A. Hosseini, L. Karlsson, S. Wessman, N. Fuertes, Effect of σ phase morphology on the degradation of properties in a super duplex stainless steel, Materials 11 (2018) 933, https://doi.org/10.3390/ma11060933.

[16] D.G. Lee, J.H. Kim, S.H. Kim, H.Y. Ha, T.H. Lee, J. Moon, D.W. Suh, Hydrogen trapping characteristics and mechanical degradation in a duplex stainless steel, Met. Mater. Int. 29 (2023) 126–134, https://doi.org/10.1007/s12540-022-01212-w.

[17] D.C. Blaine, S.J. Park, P. Suri, R.M. German, Application of work-of-sintering concepts in powder metals, Metall. Mater. Trans. 37 (2006) 2827–2835, https://doi.org/10.1007/BF02586115.

[18] A.P. Zhilyaev, T.G. Langdon, Using high-pressure torsion for metal processing: fundamentals and applications, Prog. Mater. Sci. 53 (2008) 893–979, https://doi.org/10.1016/j.pmatsci.2008.03.002.

[19] B. Verlee, T. Dormal, J. Lecomte-Beckers, Density and porosity control of sintered 316L stainless steel parts produced by additive manufacturing, Powder Metall. 55 (2012) 260–267, https://doi.org/10.1179/0032589912Z.00000000082.

[20] P. Sathiyamoorthi, P. Asghari-Rad, J.W. Bae, H.S. Kim, Fine tuning of tensile properties in CrCoNi medium entropy alloy through cold rolling and annealing, Intermetallics 113 (2019) 106578, https://doi.org/10.1016/j.intermet.2019.106578.

[21] P. Zhang, W. Han, Z. Huang, G. Li, M. Zhang, J. Li, Microstructure evolution and corrosion behavior of 316L stainless steel subjected to torsion, Mater. Res. Express 8 (2021) 086519, https://doi.org/10.1088/2054-1591/ac1ecc.

[22] D.N. Lee, Strain energy release maximization model for recrystallization textures, Met. Mater. Int. 5 (1999) 301–417, https://doi.org/10.1007/BF03026153.

[23] M. El-Tahawy, P.H.R. Pereira, Y. Huang, H. Park, H. Choe, T.G. Langdon, J. Gubicza, Exceptionally high strength and good ductility in an ultrafine-grained 316L steel processed by severe plastic deformation and subsequent annealing, Mater. Lett. 214 (2018) 240–242, https://doi.org/10.1016/j.matlet.2017.12.040.

[24] J.S. Li, G.J. Cheng, H.W. Yen, L.T. Wu, Y.L. Yang, R.T. Wu, J.-R. Yang, S.H. Wang, Thermal cycling induced stress-assisted sigma phase formation in super duplex stainless steel, Mater. Des. 182 (2019) 108003, https://doi.org/10.1016/j.matdes.2019.108003.

[25] K. Saeidi, S. Alvi, F. Lofaj, V.I. Petkov, F. Akhtar, Advanced mechanical strength in post heat treated SLM 2507 at room and high temperature promoted by hard/ductile sigma precipitates, Metals 9 (2019) 199, https://doi.org/10.3390/met9020199.

[26] C.C. Hsieh, W. Wu, Overview of intermetallic σ phase precipitation in stainless steels, ISRN Metall 16 (2012) 732471, https://doi.org/10.5402/2012/732471.

[27] G.S. Fonseca, P.S.N. Mendes, A.C.M. Silva, Sigma phase: nucleation and growth, Metals 9 (2019) 34, https://doi.org/10.3390/met9010034.

[28] D.M.E. Villanueva, F.C.P. Junior, R.L. Plaut, A.F. Padilha, Comparative study on sigma phase precipitation of three types of stainless steels: austenitic, superferritic and duplex, Mater. Sci. Technol. 22 (2016) 9, https://doi.org/10.1179/174328406X109230.

[29] F. Tang, J.M. Schoenung, Strain softening in nanocrystalline or ultrafine-grained metals: a mechanistic explanation, Mater. Sci. Eng. 493 (2008) 101–103, https://doi.org/10.1016/j.msea.2007.08.086.

[30] H. Li, S. Gao, Y. Tomota, S. Ii, N. Tsuji, T. Ohmura, Mechanical response of dislocation interaction with grain boundary in ultrafine-grained interstitial-free steel, Acta Mater. 206 (2021) 116621, https://doi.org/10.1016/j.actamat.2021.116621.

[31] S.J. Sun, Y.Z. Tian, H.R. Lin, X.G. Dong, Y.H. Wang, Z.J. Zhang, Z.F. Zhang, Enhanced strength and ductility of bulk CoCrFeMnNi high entropy alloy having fully recrystallized ultrafine-grained structure, Mater. Des. 133 (2017) 122–127, https://doi.org/10.1016/j.matdes.2017.07.054.

[32] Y. Huang, T.G. Langdon, Advances in ultrafine-grained materials, Mater. Today 16 (2013) 85–93, https://doi.org/10.1016/j.mattod.2013.03.004.

[33] M. Rostami, R. Miresmaeili, A.H. Astaraee, Investigation of surface nanostructuring, mechanical performance and deformation mechanisms of AISI 316L stainless steel treated by surface mechanical impact treatment, Met. Mater. Int. (2022), https://doi.org/10.1007/s12540-022-01286-6.

[34] L. Zhang, Z. Hu, L. Zhang, H. Wang, J. Li, Z. Li, J. Yu, B. Wu, Enhancing the strength-ductility trade-off in a NiCoCr-based medium-entropy alloy with the synergetic effect of ultrafine precipitates, stacking faults, dislocation locks and twins, Scripta Mater. 211 (2022) 114497, https://doi.org/10.1016/j.scriptamat.2021.114497.

[35] X. Wang, X. Pan, P. Sun, C. Qiu, Significant enhancement in tensile strength and work hardening rate in CoCrFeMnNi by adding TiAl particles via selective laser melting, Mater. Sci. Eng. 831 (2022) 142285, https://doi.org/10.1016/j.msea.2021.142285.

[36] M. Liu, W. Gong, R. Zheng, J. Li, Z. Zhang, S. Gao, C. Ma, N. Tsuji, Achieving excellent mechanical properties in type 316 stainless steel by tailoring grain size in homogeneously recovered or recrystallized nanostructures, Acta Mater. 226 (2022) 117629, https://doi.org/10.1016/j.actamat.2022.117629.

[37] Q. Zhou, J. Liu, Y. Gao, An insight into oversaturated deformation-induced sigma precipitation in Super304H austenitic stainless steel, Mater. Des. 181 (2019) 108056, https://doi.org/10.1016/j.matdes.2019.108056.

[38] M.V. Biezma, U. Martin, P. Linhardt, J. Ress, C. Rodriguez, D.M. Bastidas, Non-destructive techniques for the detection of sigma phase in duplex stainless steel: a comprehensive review, Eng. Fail. Anal. 122 (2021) 105227, https://doi.org/10.1016/j.engfailanal.2021.105227.

[39] G. Laplanche, Growth kinetics of σ-phase precipitates and underlying diffusion processes in CrMnFeCoNi high-entropy alloys, Acta Mater. 199 (2020) 193–208, https://doi.org/10.1016/j.actamat.2020.08.023.

[40] Y.Z. Tian, J. Freudenberger, R. Pippan, Z.F. Zhang, Formation of nanostructure and abnormal annealing behavior of a Cu-Ag-Zr alloy processed by high-pressure torsion, Mater. Sci. Eng. 568 (2013) 184–194, https://doi.org/10.1016/j.msea.2012.11.048.

[41] D.H. Lee, J.A. Lee, Y. Zhao, Z. Lu, J.Y. Suh, J.Y. Kim, U. Ramamurty, M. Kawasaki, T.G. Langdon, J. Jang, Annealing effect on plastic flow in nanocrystalline CoCrFeMnNi high-entropy alloy: a nanomechanical analysis, Acta Mater. 140 (2017) 443–451, https://doi.org/10.1016/j.actamat.2017.08.057.

[42] L.X. Sun, N.R. Tao, M. Kuntz, J.Q. Yu, K. Lu, Annealing-induced hardening in a nanostructured low-carbon steel prepared by using dynamic plastic deformation, J. Mater. Sci. Technol. 30 (8) (2014) 731–735, https://doi.org/10.1016/j.jmst.2014.03.008.

[43] R. Song, D. Ponge, D. Raabe, Improvement of the work hardening rate of ultrafine grained steels through second phase particles, Scripta Mater. 52 (2005) 1075–1080, https://doi.org/10.1016/j.scriptamat.2005.02.016.

[44] N. Moelans, B. Blanpain, P. Wollants, Pinning effect of second-phase particles on grain growth in polycrystalline films studied by 3-D phase field simulations, Acta Mater. 55 (2007) 2173–2182, https://doi.org/10.1016/j.actamat.2006.11.018.

[45] H. Zhou, Y. Lin, F. Chen, Q. Shen, Effect of precipitation behavior on mechanical properties of a Nb-containing CoCrNi-based high-entropy alloy, Met. Mater. Int. 29 (2023) 674–692, https://doi.org/10.1007/s12540-022-01265-x.

[46] S. Chen, G. Ma, G. Wu, A. Godfrey, T. Huang, X. Huang, Strengthening mechanisms in selective laser melted 316L stainless steel, Mater. Sci. Eng. 823 (2022) 142434, https://doi.org/10.1016/j.msea.2021.142434.

[47] H. Kwon, J. Moon, J.W. Bae, J.M. Park, S. Son, H.S. Do, B.J. Lee, H.S. Kim, Precipitation-driven metastability engineering of carbon-doped CoCrFeNiMo medium-entropy alloys at cryogenic temperature, Scripta Mater. 188 (2020) 140–145, https://doi.org/10.1016/j.scriptamat.2020.07.023.

[48] D. Yim, P. Sathiyamoorthi, S.J. Hong, H.S. Kim, Fabrication and mechanical properties of TiC reinforced CoCrFeMnNi high-entropy alloy composite by water atomization and spark plsma sintering, J. Alloys Compd. 781 (2019) 389–396, https://doi.org/10.1016/j.jallcom.2018.12.119.

[49] B.P. Kashyap, K. Tangri, On the Hall-Petch relationship and substructural evolution in type 316L stainless steel, Acta Metall. Mater. 43 (11) (1995) 3971–3981, https://doi.org/10.1016/0956-7151(95)00110-H.

[50] Z. Yanushkevich, S.V. Dobatkin, A. Belyakov, R. Kaibyshev, Hall-Petch relationship for austenitic stainless steels processed by large strain warm rolling, Acta Mater. 136 (2017) 39–48, https://doi.org/10.1016/j.actamat.2017.06.060.

[51] N. Hansen, X. Huang, Microstructure and flow stress of polycrystals and single crystals, Acta Mater. 46 (5) (1998) 1827–1836, https://doi.org/10.1016/S1359-6454(97)00365-0.

[52] T. Ungar, A.D. Stoica, G. Tichy, X.-L. Wang, Orientation-dependent evolution of the dislocation density in grain populations with different crystallographic orientations relative to the tensile axis in a polycrystalline aggregate of stainless steel, Acta Mater. 66 (2014) 251–261, https://doi.org/10.1016/j.actamat.2013.11.012.

[53] M. El-Tahawy, Y. Huang, T. Um, H. Choe, J.L. Labar, T.G. Langdon, J. Gubicza, Stored energy in ultrafine-grained 316L stainless steel processed by high-pressure torsion, J. Mater. Res. Technol. 6 (4) (2017) 339–347, https://doi.org/10.1016/j.jmrt.2017.05.001.

[54] M. Tikhonova, N. Enikeev, R.Z. Valiev, A. Belyakov, R. Kaibyshev, Submicrocrystalline austenitic stainless steel processed by cold or warm high pressure torsion, Mater. Sci. Forum 838–839 (2016) 398–403, https://doi.org/10.4028/www.scientific.net/MSF.838-839.398.

[55] Q. lin, X. An, H. Liu, Q. Tang, P. Dai, X. Liao, In-situ high-resolution transmission electron microscopy investigation of grain boundary dislocation activities in a nanocrystalline CrMnFeCoNi high-entropy alloy, J. Alloys Compd. 709 (2017) 802–807, https://doi.org/10.1016/j.jallcom.2017.03.194.

[56] H. Kwon, P. Asghari-Rad, J.M. Park, P. Sathiyamoorthi, J.W. Bae, J. Moon, A. Zargaran, Y.T. Choi, S. Son, H.S. Kim, Synergetic strengthening from grain refinement and nano-scale precipitates in non-equiatomic CoCrFeNiMo medium-entropy alloy, Intermetallics 135 (2021) 107212, https://doi.org/10.1016/j.intermet.2021.107212.